Transport of tungsten in the H-mode edge transport barrier of ITER

R. Dux[1], A. Loarte[2], E. Fable[1], A. Kukushkin[2]

[1]Max-Planck-Institut für Plasmaphysik, Garching, Germany
[2]ITER Organization, Route de Vinon sur Verdon, 13115 Saint Paul Lez Durance, France

E-mail: `Ralph.Dux@ipp.mpg.de`

Abstract. The neoclassical transport of tungsten in the H-mode edge transport barrier of ITER is investigated and scaling relations for the transport coefficients are evaluated. The major finding is that the radial convection velocity of tungsten is outward directed for a large proportion of the tested pedestal profiles. This is due to a combination of the high pedestal temperatures and the high separatrix densities making the outward directed temperature screening term to be the predominant contribution of the collisional convection. The high densities at the separatrix are needed to control the power exhaust and the tungsten sputtering in the divertor and the high pedestal temperatures are expected to be achieved in ITER to meet its fusion performance objectives. The density and temperature profiles, which deliver simultaneously optimum fusion performance, power exhaust and tungsten sputtering control in ITER, also ensure optimum collisional radial transport of tungsten leading to hollow tungsten density profiles in the edge transport barrier. In helium H-mode plasmas, which are considered for the initial ITER non-active operation, this very favourable neoclassical transport effect is reduced and only about half of the considered edge plasma profiles yield an outward directed drift.

PACS numbers: 52.55.Fa, 52.25.Fi, 52.25.Vy

1. Introduction

Even though the erosion rates of tungsten (W) are much lower than for the light elements, the risk of high central power losses by radiation, which can affect both fusion reactivity and edge power flow (thus leading to the loss of H-mode confinement), is still inherent in the use of W as a divertor material in ITER. The penetration of W into the central plasma depends on many mechanisms: prompt redeposition, transport of W ions parallel to the magnetic field out of the divertor volume, and radial transport across the separatrix and further into the core of the plasma. An important element is the transport of tungsten in the edge transport barrier (ETB) of H-mode plasmas.

Analyses of the impurity transport in the ETB region of H-mode plasmas on ASDEX [1], JET [2, 3, 4, 5], DIII-D [6], Alcator C-Mod [7, 8], and ASDEX Upgrade [9, 10] show, that the transport of impurities is characterised by a suppressed diffusion and, typically, a strong inward convection. In H-mode plasmas without edge localised modes (ELM), it was found, that the assumption of an inward drift is indispensable to explain the rapid rise of impurity radiation [1, 2], the observed shape of the total [3] and soft X-ray(SXR) radiation [8] and the SXR and VUV radiation from injected impurities using Laser Blow-Off [4, 5, 7]. In H-Mode plasmas with type-I ELMs, analysis of soft X-ray measurements in ASDEX Upgrade [9] found a strong peaking of neon in the ETB, which is effectively flattened during each ELM. The diffusion between ELMs was again found to be low but a direct comparison with neoclassical theory was not possible at that time due to the missing ion temperature profiles.

The above mentioned investigations were in some respect indirect, since they were not based on a measurement of the impurity density evolution in the H-mode barrier, which has to be detected with very high spatial resolution of a few mm on a dense grid of measurement points to resolve the large gradients. With the help of high resolution charge exchange recombination spectroscopy(CXRS) [11], direct measurements of the impurity transport coefficients in this region could be performed in ASDEX Upgrade by analysing the density profile evolution of helium, carbon, neon and argon [10]. It was found that between ELMs, all impurities are subject to an inward pinch leading to steep impurity density gradients which are flattened during ELMs. The evaluated impurity transport coefficients between ELMs were in accordance with neoclassical theory. The ratio of the inward pinch velocity v to the diffusion coefficient D was increasing with impurity charge Z and caused an increase in the peaking with increasing impurity charge.

Based on this experimental evidence, it can be reasonably assumed that W transport in the ETB in the phase between ELMs will be appropriately described by neoclassical theory. The large pedestal temperatures in ITER cause tungsten to attain quite high charge states with Z in the range of 50 and, thus, the v/D ratios are expected to be very high in the edge transport barriers of ITER plasmas. For the ITER reference scenario for inductive operation with fusion gain Q=10 (toroidal magnetic field B_T=5.3 T, plasma current I_p=15 MA), neoclassical transport parameters

have been calculated for one specific set of profiles for electron density n_e, electron temperature T_e and ion temperature T_i [12]. The neoclassical diffusion coefficient D_{neo} of W was in the range 0.01-0.03 $\mathrm{m^2 s^{-1}}$ and the drift velocity was inwardly directed with values around $v_{neo}/D_{neo} \approx$ -50 $\mathrm{m^{-1}}$. However, the chosen electron density profile in [12] had a very low density at the separatrix n_{sep}=1.9×10^{19} $\mathrm{m^{-3}}$, which is not compatible with detached divertor operation for these ITER plasma conditions [13], while profiles with higher values of n_{sep} would yield much less inward pinch or an outward directed drift. As discussed in the next section, the drift velocity is proportional to the difference of the logarithmic density gradient and temperature gradient and a substantial reduction in the normalised density gradient can lead to reversal of the drift direction.

In this paper, we therefore undertake a more methodical approach to study the neoclassical transport of W in the edge transport barrier of ITER. Here, we produce a large range of pedestal profiles of electron density and temperature using a simple parametrisation of the respective edge profiles containing wide, narrow, high, and low pedestal values and all possible combinations for temperature and density. For each profile, the neoclassical transport parameters are calculated and the goal is to develop easily applicable scaling expressions for the diffusion coefficient D_{neo} and the effective temperature screening factor H_{eff}, i.e. the ratio of normalised density gradient and normalised temperature gradient which leads to a zero drift velocity of tungsten. With the scaling of H_{eff}, the average neoclassical drift v_{neo} in the ETB can be evaluated and the parameter space, which yields inward or outward drift, can be quantified.

In an H-mode plasma, the temporal phases with neoclassical transport between ELMs alternate with short phases with strongly increased transport during ELMs. The power and particle fluxes deposited on the plasma facing components during ELMs lead to a large increase of the tungsten erosion at the plasma facing components, which is found to dominate the time averaged tungsten erosion in present experiments, i.e. including erosion by ELMs and inter-ELMs [14, 12, 15]. An analysis of this dynamical situation for ITER has been performed using transport calculations including impurity transport and will be reported elsewhere [16]. Dust [17] might be another source of plasma contamination by tungsten which is outside the scope of this study.

The paper is organised as follows. In section 2, we shortly review the theory of the neoclassical impurity transport and describe the code that we have used to calculate the neoclassical transport coefficients at the edge of the ITER plasmas. In section 3 we describe the parametrisation of the edge profiles based on the pedestal and separatrix values for temperature and density and a pedestal width parameter. In section 4, the radial profiles of the neoclassical transport parameters of W are discussed for two typical parameter sets of the scan, where we concentrate on the profile of the drift parameter v/D which either provokes a peaking or a reduction of the W-density across the ETB region. It is shown there, that when all other parameters are kept fixed, there is always one separatrix density that leads to a flat W-profile across the ETB for the pedestal plasma characteristics expected in ITER reference operational scenarios. The calculation of this separatrix density is the main result of this paper and is discussed in

section 5. In addition, we derive a scaling for the diffusion coefficient for W transport in ITER pedestal plasmas in section 6. The sensitivity of the results obtained in our study with respect to the chosen impurity composition is found to be rather low and this is discussed in section 7. A specific physics issue related to the reduction and even reversal of the temperature screening at very high-collisionalities is discussed in section 8. Helium plasmas in H-mode are foreseen for the non-active phase of initial ITER operation. He H-mode plasmas in ITER will have a lower level of heating power than DT H-mode plasmas due to possible limitations in the power of the additional heating systems initially available and because the lack of alpha heating [18]. He H-mode plasmas have generally higher collisionality than similar DT plasmas and the reduced temperature screening leads to a less favourable neoclassical transport of W in the ETB. This will be described in section 9 before concluding in section 10.

2. Neoclassical impurity transport

In neoclassical theory, the flux surface average of the radial flux density $\langle \Gamma_a^r \rangle$ of species a with charge q_a is caused by the toroidal component of the friction forces $\vec{F}_{ab}$ between a and all other species: $\langle \Gamma_a^r \rangle = \sum_b \langle \Gamma_{ab}^r \rangle \propto (1/q_a) \sum_b \langle R F_{ab,t} \rangle$, where R is the major radius [19, 20]. $\vec{F}_{ab}$ equals $-\vec{F}_{ba}$ due to momentum conservation and the flux components satisfy $q_a \langle \Gamma_{ab}^r \rangle + q_b \langle \Gamma_{ba}^r \rangle = 0$. This balance of the radial fluxes assures ambipolarity of the total flux: $\sum_a q_a \langle \Gamma_a^r \rangle = 0$. The toroidal friction forces can be split into perpendicular and parallel components leading to the classical(CL), Pfirsch-Schlüter(PS) and Banana-Plateau(BP) contribution and also the fluxes of each component alone are balanced and thus ambipolar. Each contribution has a diffusive and a convective term and, for equal temperatures of all species, one can formally write [19, 21, 22].

$$\langle \Gamma_a^r \rangle = \sum_{x=CL,PS,BP} \sum_{b \neq a} D_x^{ab} \left[-\frac{dn_a}{dr} + \frac{Z_a}{Z_b} \left(\frac{d \ln n_b}{dr} - H_x^{ab} \frac{d \ln T}{dr} \right) n_a \right] \tag{1}$$

Thus, the total neoclassical diffusion coefficient D_{neo} and the total drift velocity v_{neo} of species a is:

$$D_{neo} = \sum_{x=CL,PS,BP} \sum_{b \neq a} D_x^{ab}$$

$$v_{neo} = \sum_{x=CL,PS,BP} \sum_{b \neq a} D_x^{ab} \frac{Z_a}{Z_b} \left(\frac{d \ln n_b}{dr} - H_x^{ab} \frac{d \ln T}{dr} \right) \tag{2}$$

The diffusion coefficients D_x^{ab} and the temperature screening factors H_x^{ab} depend on plasma parameters such as density, temperature, magnetic field and flux surface geometry but not on the gradients of temperature and density. The drift velocity of each contribution is proportional to the respective diffusion coefficient multiplied with the ratio of the charge numbers Z_a/Z_b. In the low collisionality regime, the Banana-Plateau terms contribute most to the total flux, while the high collisionality regime is dominated by Pfirsch-Schlüter transport. In eq.(1) and (2), the contribution from electrons can be

neglected due to the small friction force. The impurity strength parameter

$$\alpha = Z_I^2 n_I/(Z_m^2 n_m) \tag{3}$$

can be used to judge the importance of impurity-impurity collisions. Z_I and n_I are charge number and density of the impurity, while Z_m and n_m are the respective quantities for the main ion. In the trace limit, where $\alpha \ll 1$ for all impurities in the plasma, it is only necessary to consider collisions with the main ion, while for $\alpha \approx 1$ collisions with impurities have to be considered as well.

For the case with zero impurity neutral sources inside the separatrix, the impurity density profile in temporal equilibrium only depends on the ratio of drift velocity and diffusion coefficient, i.e. $1/n_a(dn_a/dr) = d\ln n_a/dr = v_{neo}/D_{neo}$. In the trace limit, where only collisions with the main ion need to be considered, we find from eq.(2) the relation between impurity density gradient and main ion density gradient in equilibrium.

$$\frac{d\ln n_a}{dr} = \frac{d\ln n_m}{dr}\frac{Z_a}{Z_m}\left(1 - \frac{\sum_x H_x^{am} D_x^{am}}{\sum_x D_x^{am}}\frac{d\ln T}{d\ln n_m}\right) = \frac{d\ln n_m}{dr}\frac{Z_a}{Z_m}\left(1 - H_{av}\eta_m\right) \tag{4}$$

Here, η_m denotes the ratio of normalised temperature gradient and normalised main ion density gradient and $H_{av} = \sum_x H_x^{am} D_x^{am}/\sum_x D_x^{am}$ is the average temperature screening factor of all three (CL, PS and BP) contributions. For zero temperature gradient, the normalised impurity density gradient is a factor Z_a/Z_m steeper than the normalised main ion density gradient. For tungsten, Z_a is especially large in the edge transport barrier. This can lead to very large tungsten density gradients in the ETB and thus to very large values of the W impurity concentration in the core plasma (inside the ETB) for modest values of W impurity concentration at the separatrix. The concern about the existence of such strongly peaked tungsten profiles in the ETB of ITER reference operational scenarios is the main motivation for the study presented in this paper. For a non-zero temperature gradient, this factor is reduced, since η_m is positive (same direction of both gradients) and H_{av} is positive. H_{CL}^{am} and H_{PS}^{am} are always positive and have lower absolute values for the light elements than for heavy elements. H_{BP}^{am} is positive in the low collisionality regime, where D_{BP}^{am} is the dominant diffusion contribution, and becomes negative for increasing collisionality ν_a^*. However, the effective value H_{av} remains positive in all collisionality regimes. Deep in the PS-regime, there is a reduction of H_{PS}^{am}. This is due to the strong collisional coupling of impurity and main ion, which leads to energy transfer from impurity ion onto main ion on the upper and lower part of the flux surface. Thus, the temperature variation for the impurity ion along the flux surface and the corresponding temperature screening term is reduced and eventually changes sign at extremely high collisionalities (see eq.(6.72-75) in [19] and [23]). We have calculated the collisionality at which the reversal of the temperature drift occurs in ITER and will discuss it in section 8.

The neoclassical transport coefficients of impurities were calculated with the NEOART code developed by A. G. Peeters [23]. NEOART calculates the collisional transport coefficients for an arbitrary number of impurities including collisions between

all components. The velocity distribution is expanded in the three first Laguerre polynomials of order 3/2, which are used to define 'velocities'. The first 'velocity' is the mean particle velocity of the component, the second proportional to the heat flow, while the third term in the expansion is not related to well known quantities. For the neoclassical part, the code solves the set of linear coupled equations for the parallel 'velocities' in arbitrary toroidally symmetric geometry for all collision regimes. The classical fluxes are given by eq.(5.9) and (5.10) in section 5 of Hirshman and Sigmar [19]. The equations for the banana plateau contribution are equal to those used by Houlberg [24]. The Pfirsch-Schlüter contribution is calculated from the coupled equations (6.1-2) and (6.14-15) of Hirshman and Sigmar [19], as described in Ref. [23]. NEOART applies the reduced charge state formalism [19], which is the correct way to merge the different charge states of one species, such that the matrices that have to be inverted are only determined by the number of species instead of all charge states of the atoms.

We have performed calculations with a stand-alone version of NEOART that yields for all impurity species the diffusion coefficients D_{neo} and the drift velocities v_{neo} for a given magnetic equilibrium, given profiles of electron and ion temperatures and profiles of the density of all species. After the necessary preparation work, the actual computation time is rather fast and many different profiles can be analysed. With such calculations, the influence of many parameters on the direction of the neoclassical drifts (inward or outward) and on the magnitude of the diffusion coefficient can be studied in detail.

The magnetic equilibrium for the reference ITER inductive scenario with $Q = 10$ ($B_T = 5.3\,\mathrm{T}$ and $I_p = 15\,\mathrm{MA}$, $q_{95} \approx 3$) was taken from CORSICA simulations [25]. From the poloidal flux Ψ on the given R, Z-grid for this equilibrium, the flux surfaces were reconstructed and the necessary flux surface averages of the magnetic fields and the trapped particle fraction were calculated. The outermost flux surface, which was used here, had a normalised poloidal flux $\rho_{pol} = 0.999$, where we use

$$\rho_{pol} = \sqrt{\frac{\Psi - \Psi_{axis}}{\Psi_{sep} - \Psi_{axis}}} \tag{5}$$

From the volume V enclosed by each flux surface the radial coordinate r is defined.

$$r = \sqrt{\frac{V}{2\pi^2 R_{axis}}} \tag{6}$$

Thus, r is the radius of a cylinder with length $2\pi R_{axis}$ and with the same volume V as enclosed by the flux surface contour (unit = [m]). All transport coefficients and gradients in this paper are given with respect to this radial coordinate. Furthermore, we use the co-ordinate x, which is the distance to the separatrix as measured at the low-field side on a horizontal chord through the magnetic axis, i. e. $x = R_{lfs,sep} - R_{lfs}$ at $Z = Z_{mag}$. For other ITER plasma scenarios, as the region of interest for our study is the ETB, it was found sufficient to apply a simple linear scaling of Ψ with I_p and of the toroidal field to obtain the magnetic equilibria for other ITER H-mode scenarios with other plasma current and toroidal field levels.

3. Parametric Scan of Pedestal Parameters

The neoclassical transport of W was studied for a large range of pedestal profiles of electron density and temperature at various values of plasma current and toroidal field. The parametrisation of the electron density $n_e(x)$ in the edge pedestal region uses the pedestal density n_{ped}, the separatrix density n_{sep} and the characteristic density pedestal width w_n.

$$n_e(x) = \frac{n_{ped} + n_{sep}}{2} + \frac{n_{ped} - n_{sep}}{2} \; \frac{\tanh(2x/w_n - 1)}{\tanh(1)} \qquad (7)$$

For the temperature $T(x)$, the parametrisation has the same form for $x < w_T$.

$$T_{<w_T}(x) = \frac{T_{ped} + T_{sep}}{2} + \frac{T_{ped} - T_{sep}}{2} \; \frac{\tanh(2x/w_n - 1)}{\tanh(1)} \quad \text{for} \quad x < w_T \qquad (8)$$

Just one temperature $T=T_e=T_i$ is used. For the neoclassical transport, only T_i is of importance, while T_e enters indirectly via the charge distribution of tungsten. The mean temperature is close to T_i in the ITER main plasma (including most of the ETB) because of the large ratio of the expected energy confinement time to the typical timescale for equipartition. Only close to the separatrix T_i is significantly above T_e in ITER [13]. Therefore, a T_{sep} of roughly $1.5{\times}T_{e,sep}$ was used in our study. $T(x)$ continues as a linearly increasing function further inward.

$$T_{>w_T}(x) = T_{ped} + (T_{axis} - T_{ped}) \; \frac{x - w_T}{a - w_T} \quad \text{for} \quad x > w_T \qquad (9)$$

Here, T_{axis} is the temperature on axis, which is at a distance a to the separatrix. In order to avoid a discontinuity of the temperature gradient at $x = w_T$, we used a smooth transition of the two temperature functions within $w_T/5$ around $x=w_T$ using:

$$T(x) = (1 - f(x))T_{<w_T}(x) + f(x)T_{>w_T}(x) \quad \text{with} \quad f(x) = \frac{1 + \tanh[10(x/w_T - 1)]}{2} \qquad (10)$$

For each combination of the toroidal field B_T and plasma current I_p considered, three values of the pedestal width and height for the density and temperature were studied, so that 81 combinations were evaluated per (B_T, I_p).

w_T [cm]	T_{ped} [keV]	T_{sep} [keV]	T_{axis} [keV]	w_n [cm]	n_{ped} $[10^{19}\text{m}^{-3}]$	n_{sep} $[n_{ped}]$
3,**6**,9	3,**4.5**,6	0.3	22	3,**6**,9	6.5,**8**,9.5	$\approx$0.2-0.8

Table 1. Range of scanned parameters for a DT-plasma at I_p=15 MA and B_T=5.3 T.

The values considered for a DT-plasma with I_p=15 MA and B_T=5.3 T are shown in Tab.1. These cover the range of pedestal parameters which are required to achieve the Q=10 fusion performance in ITER [25] and which are compatible with the limits imposed by edge MHD stability [26]. The range of pedestal widths considered corresponds to

that expected from empirical extrapolations of present experimental results, which are assumed not to depend on the values of plasma current and toroidal field [27]. For each parameter combination, the neoclassical transport parameters were calculated for ten values of n_{sep}. This procedure was repeated for 5.3 T and 7.5, 10 and 12.5 MA. These correspond to the stationary phases of the foreseen ITER high Q scenarios (15MA for Q=10 and 12.5MA for the long pulse Q=5 scenario based on hybrid H-mode performance) and to intermediate H-mode scenarios to be developed to access these scenario in the ITER Research Plan or ramp-up/down H-mode phases in them [18]. In addition, 7.5 MA at half field of 2.65 T H-modes have also been modelled. These correspond to H-mode plasmas expected to be explored in the non-active phase (in He plasmas, see section 9) and in the initial phase of DD/DT operation [18]. Here, the values for n_{ped}, T_{ped} and T_{axis} have been scaled linearly with I_p to have a constant Greenwald fraction and a pedestal pressure and overall plasma confinement that scales with I_p as seen in experiment. The exact scaling of these parameters is not so important since it just sets the boundaries for the scanned parameter range, which anyway is rather wide. For the separatrix temperature, its scaling was based on dominant parallel heat conduction with a power decay length λ_q that scales with I_p^{-1} [28]. Starting from $T_{sep} \propto (L_{con}q_\parallel)^{2/7} \propto (P_{SOL}L_{con}/A_{q\parallel})^{2/7}$ and $A_{q\parallel} \approx 4\pi R\lambda_q B_p/B_T$, this yields a scaling $T_{sep} \propto P_{SOL}^{2/7}B_T^{4/7}I_p^{-2/7}$. Furthermore, we assumed a constant fraction of core radiation, such that the power crossing the separatrix P_{SOL} is proportional to the sum of the powers by additional heating and α-heating. In the development of this scaling, the additional heating power was fixed at a level of 50 MW and the α-heating was assumed to scale with I_p^3 (resulting from $P_\alpha \propto W_{plasma}^2$ and $W_{plasma} \propto I_p^{1.5}$ according to the ITER-H98(y,2) scaling law for energy confinement [29]) and to provide 100 MW at I_p=15 MA. These settings lead to:

$$T_{sep}(I_p, B_T) = T_{sep}(15MA, 5.3T)(\frac{B_T}{5.3\text{T}})^{4/7}(\frac{15\text{MA}}{I_p})^{2/7}(\frac{5 + 10(I_p/15\text{MA})^3}{15})^{2/7} \quad (11)$$

The main ion species was a 50/50 mix of D and T and the impurity composition was He(2%), Be(2%), Ar(0.1%) and W(5×10^{-6}) with radially constant impurity concentrations n_{imp}/n_e. The concentrations of He and Be are typical values considered for ITER scenario simulations [30], the concentration of Ar is a typical value for radiatively cooled plasmas [31] and W was chosen to have a low concentration at the trace level. The impurity strength parameters of eq.(3) are $\alpha_{\text{He}}\approx0.1$, $\alpha_{\text{Be}}\approx0.4$, $\alpha_{\text{Ar}}\approx0.4$, and $\alpha_{\text{W}}\approx0.01$ (using Z_{W}=45). Thus, collisions of tungsten with impurities are almost as important as collisions with the main ions.

The charge distribution is approximated by the corona distribution taking the atomic data for electron impact ionisation, radiative and di-electronic recombination from the ADAS data base [32]. Helium and beryllium are always fully ionised. The radial profiles for the mean charge of argon and tungsten are depicted in the middle box of Fig.1 for the outer 11 cm of the plasma. These profiles are given for a case with low electron temperature (blue lines), corresponding to a 7.5 MA ITER H-mode, and for
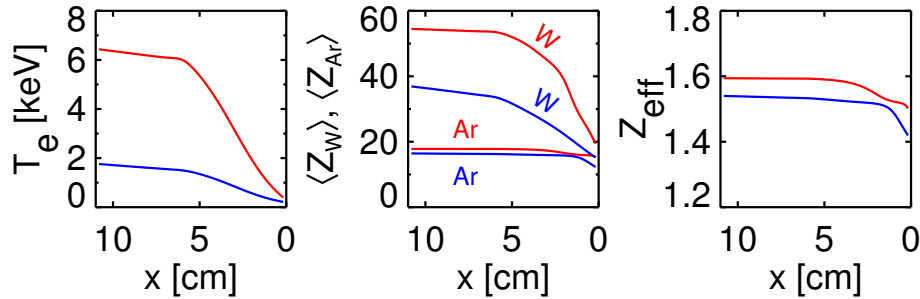
Figure 1. Two extreme cases for the pedestal temperatures and corresponding profiles of the mean charge of W and Ar and of Z_{eff}. Be and He are fully ionised.

a parameter set with high T_e (red lines), corresponding to a 15 MA ITER H-mode as shown in the left box of Fig.1. Z_{eff} is shown in the right panel for the two temperature profiles. Z_{eff} is ≈1.6 for the higher temperature case and a bit lower for the plasma with lower temperature. These Z_{eff} values are compatible with those required to achieve $Q=10$ in 15 MA ITER H-modes [25].

4. Radial Profiles for two parameter sets of the scan

Fig.2 shows the pedestal profiles of temperature, density and resulting transport coefficients of tungsten for a 15MA/5.3T case (black line) and a 7.5MA/5.3T case (red dashed lines). The profile parameters are at the central values of the parameter space, i.e. at the bold values in Tab.1 and the corresponding scaled values for the 7.5MA case. For n_{sep}, the values are $3.1 \times 10^{19}\,\mathrm{m}^{-3}$ and $2.1 \times 10^{19}\,\mathrm{m}^{-3}$ respectively.

With regard to the impurity transport coefficients, we just concentrate on the behaviour of tungsten. The collisionality ν^* of W is in the Pfirsch-Schlüter (PS) regime as indicated in the upper right box, where $\nu^* \epsilon^{3/2}$ (ϵ is the inverse aspect ratio) is far above the PS-limit of 1. Thus, the collisional transport of W is dominated by the classical and Pfirsch-Schlüter contribution, while the banana-plateau transport is small. The diffusion coefficient rises with collisionality and is on average $1.7 \times 10^{-2}\,\mathrm{m^2 s^{-1}}$ for the high current plasma and $4.2 \times 10^{-2}\,\mathrm{m^2 s^{-1}}$ for the low current case. The drift velocity v_{neo} is outward (positive) at the edge, inward around $x=5\,\mathrm{cm}$ and again outward further in as can be seen from the plot of v_{neo}/D_{neo} in the lower middle box. In temporal equilibrium, v_{neo}/D_{neo} equals the normalised density gradient of tungsten and the integral of v_{neo}/D_{neo} across the radial range of the ETB delivers the ratio of the tungsten densities at the edges of the radial interval

$$f_W = \frac{n_W(r_{top})}{n_W(r_{edge})} = \exp\Big[\int_{r_{edge}}^{r_{top}} \frac{v_{neo}dr}{D_{neo}}\Big] \qquad (12)$$

For the v_{neo}/D_{neo} profiles of Fig.2, we obtain f_W=0.32 at 15 MA and 0.38 at 7.5 MA when integrating over the radial interval r=[2.527,2.320] m corresponding to
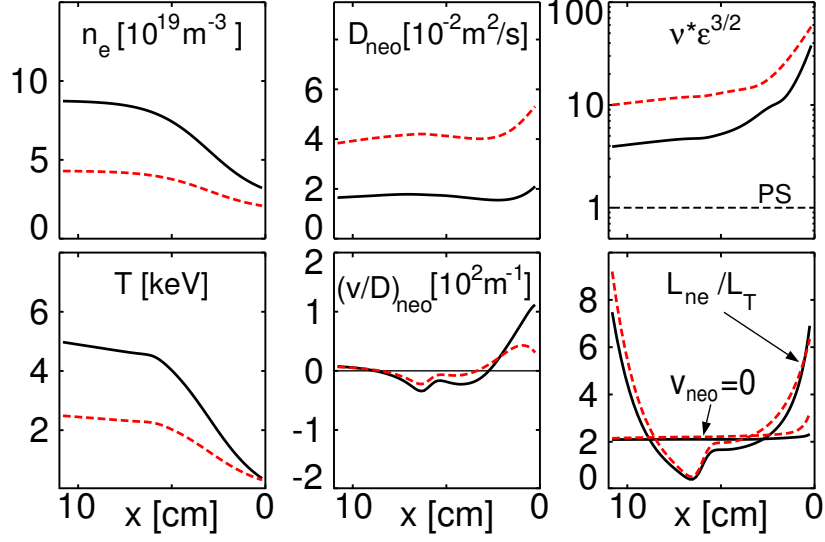
Figure 2. Pedestal profiles and collisional transport coefficients of W for 15 MA (black) and 7.5 MA (red dashed) at 5.3 T. Density and temperature parameters are as given by the bold values in Tab.1 and appropriately scaled values for 7.5 MA.

$x=[0.2,9.9]$ cm. The drift velocity of tungsten contains the sum of inward pinch contributions proportional to the normalised density gradients of main ions and light impurities and outward contribution proportional to the normalised ion temperature gradient as indicated in eq.(2). All normalised ion density gradients are approximately equal to the normalised electron density gradient due to the choice of a constant impurity concentration and due to the mild influence of the argon charge state distribution on the quasi-neutrality condition which determines the density of the main ions. The tungsten density is even lower and its effect on the main ion density gradient can be neglected. To a good approximation, the local value of v_{neo}/D_{neo} can thus be expressed as a function of the normalised electron density gradient, a mean ion charge Z_i, and a mean temperature screening factor H.

$$\frac{v_{neo}}{D_{neo}} \approx \frac{Z_W}{Z_i}\left(\frac{1}{n_e}\frac{dn_e}{dr} - H\frac{1}{T}\frac{dT}{dr}\right) \tag{13}$$

Here, Z_i is the weighted mean ion charge of all ions contributing to the collisional transport of W, where Z_i does not contain the ion charge from W itself and H is the corresponding mean temperature screening factor. More specifically, we obtain from eq.(2).

$$\frac{1}{Z_i} = \frac{1}{D_{neo}}\sum_x\sum_{b\neq W}\frac{D_x^{Wb}}{Z_b} \qquad H = \frac{\sum_x\sum_{b\neq W}\frac{D_x^{Wb}H_x^{Wb}}{Z_b}}{\sum_x\sum_{b\neq W}\frac{D_x^{Wb}}{Z_b}} \tag{14}$$

The neoclassical drift velocity of tungsten vanishes when the ratio of normalised temperature and electron density gradient L_{ne}/L_T equals $1/H$, such that the terms in the round brackets of eq.(13) add up to zero. Integrating eq.(13) from r_{edge} to r_{top}

leads to an approximate expression for f_W.

$$\ln(f_W) \approx \frac{1}{Z_i}\left(\int_{r_{edge}}^{r_{top}} Z_W \frac{d\ln n_e}{dr}dr - H\int_{r_{edge}}^{r_{top}} Z_W \frac{d\ln T}{dr}dr\right)$$

$$= \frac{1}{Z_i}\left(\langle Z_W^n\rangle \ln(f_{ne}) - H\langle Z_W^T\rangle \ln(f_T)\right)$$

$$= \frac{\langle Z_W^n\rangle}{Z_i}\left(\ln(f_{ne}) - H\frac{\langle Z_W^T\rangle}{\langle Z_W^n\rangle}\ln(f_T)\right) \quad (15)$$

Here, we have neglected the small radial variation of the mean ion charge Z_i and of the temperature screening factor H. For very high collisionalities, the temperature screening of the PS-contribution is reduced and can even reverse sign for extreme values of the collisionality. An indication of this is seen at the edge for the 7.5 MA case. The lower right box in Fig.2 shows the profile of $1/H$ for this plasma current using a red dashed line which is indicated with $v_{neo}=0$. It rises at the very edge where $\nu^*\epsilon^{3/2}$ rises towards 100. In the present parameter range, however, H does not show large excursions at the edge and H can be taken out of the integral as done in eq.(15). In contrast, the mean charge of tungsten Z_W varies strongly across the ETB and two radial averages of Z_W play an important role; these are $\langle Z_W^n\rangle$, which is an average weighted with the normalised density gradient, and $\langle Z_W^T\rangle$, which is an average weighted with the normalised temperature gradient:

$$\langle Z_W^n\rangle = \frac{\int_{r_{edge}}^{r_{top}} Z_W \frac{d\ln n_e}{dr}dr}{\int_{r_{edge}}^{r_{top}} \frac{d\ln n_e}{dr}dr} = \frac{1}{\ln(f_{ne})}\int_{r_{edge}}^{r_{top}} Z_W \frac{d\ln n_e}{dr}dr$$

$$\langle Z_W^T\rangle = \frac{\int_{r_{edge}}^{r_{top}} Z_W \frac{d\ln T}{dr}dr}{\int_{r_{edge}}^{r_{top}} \frac{d\ln T}{dr}dr} = \frac{1}{\ln(f_T)}\int_{r_{edge}}^{r_{top}} Z_W \frac{d\ln T}{dr}dr \quad (16)$$

where f_{ne} and f_T are the ratios of density and temperature at r_{top} and r_{edge}. We can therefore rewrite eq.(15) by using an approximate effective screening factor $H_{eff}^* = H\langle Z_W^T\rangle/\langle Z_W^n\rangle$, which leads to:

$$\ln(f_W) \approx \frac{\langle Z_W^n\rangle}{Z_i}\left(\ln(f_{ne}) - H_{eff}^* \ln(f_T)\right) \quad (17)$$

The lower right box of Fig.2 shows the ratio of normalised temperature and electron density gradient L_{ne}/L_T for both cases and the critical ratios $1/H$ at which the neoclassical drift velocity of tungsten is zero. The critical ratio is slightly above 2. For regions, where stronger temperature gradients lead to ratios above the critical value, the drift is outward and vice versa. For the 7.5 MA case, the critical value for zero drift velocity rises to about 3 at the edge. When increasing the separatrix density compared to the values of Fig.2, the normalised density gradient decreases and the drift direction will be predominantly outward in the ETB region. Here, a slight decrease of f_{ne} causes a strong decrease of f_W due to the high charge Z_W of tungsten. The scaling exponent is given by $\langle Z_W^n\rangle/Z_i$, where $\langle Z_W^n\rangle$ has been defined in the first line of eq.(16). For the 15 MA case, Z_W increases from 19 at the edge to 51 at the inner boundary and changes

of f_{ne} are amplified by an exponent of 14.6 leading to enormously hollow or peaked equilibrium W profiles in the ETB with small changes of the ratio of density gradients to temperature gradients (see Fig.3). For the 7.5 MA case, Z_W is a bit lower increasing from 18 to 42 and the exponent is 12. This equilibrium peaking of W is deduced from the neoclassical transport evaluated for the chosen impurity profiles; various non-linear effects have to be considered using a radial transport calculation for impurities and energy, including the effect of ELMs, to make a more precise evaluation of its magnitude for ITER, which will be reported elsewhere [16]. However, the main objective of our study is not to predict how hollow or peaked the W profile in the ETB can become but to quantify the conditions at which W neoclassical transport changes from being unfavourable (i.e peaking) to favourable (hollow) in the ETB over a wide range of ITER operational scenarios. This can provide guidance for the optimisation of ITER scenarios with respect to pedestal and separatrix plasma parameters to minimise W contamination in the inter-ELM periods. Therefore, in what follows we will determine the plasma conditions for a range of ITER scenarios which would lead to a flat tungsten profile in the ETB. For this task, we will take eq.(17) as a guideline to find a suitable scaling expression for the edge profile parameters, which coincide with a flat tungsten profile, and will use it to gain a better insight into the parameter dependences of the scaling. However, the determination of the parameter combinations, which cause $f_W = 1$, will only rely on eq.(12) and not on the approximate equations (13)-(17).

5. Scaling of the pedestal parameters leading to flat W-profiles

For each parameter set, the separatrix density was varied in fine steps and the resulting tungsten density ratio f_W was evaluated using eq.(12) for the interval x=[0.2,9.9] cm. The inner boundary of the calculations was chosen to be large enough to include the total density rise for the case with a large pedestal width of 9 cm. From this variation, the n_{sep} value leading to a flat W-profile (f_W=1) was determined. An example of such a variation of n_{sep} at otherwise constant profile parameters is shown in Fig.3. In the right graph of Fig.3, f_W is plotted versus f_{ne} on a double logarithmic scale. All other parameters are the same as for the 15 MA case of Fig.2. The points lie on a straight line as predicted by eq.(17). The slope is 14.6 corresponding to $\langle Z_W^n \rangle / Z_i$=37.7/2.58 and f_W is 1 for f_{ne}=2.92. With f_T=13.1, we obatin the critical ratio $\ln(f_{ne}) / \ln(f_T)$=0.42 at which the tungsten density profile is flat. In the spirit of the approximate eq.(17), we call this critical ratio the true effective temperature screening factor $H_{eff} = \ln(f_{ne}) / \ln(f_T)$ for this parameter set. Thus, H_{eff} was calculated for all parameter sets from the corresponding electron density and temperature ratios. H_{eff} was found to vary between 0.33 and 0.6 for all conditions explored.

     A function for H_{eff}, which yields a good fit to the data set, has only a linear dependence on the collisionality of W at the plasma edge plus a correction term that
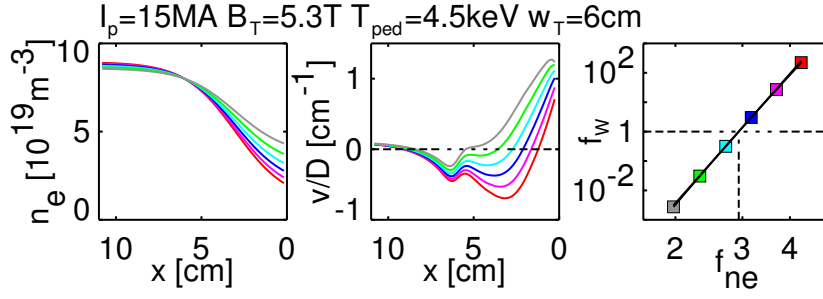
Figure 3. Example of a scan of n_{sep} from $2.0{\times}10^{19}\,\mathrm{m^{-3}}$ to $4.3{\times}10^{19}\,\mathrm{m^{-3}}$: The parameters were as given in the figure title. Density and temperature pedestal have equal width. The profiles of density and drift parameter are shown in the left and middle box for 6 values of n_{sep}. In the right graph, the corresponding tungsten density ratio is plotted versus the electron density ratio on a double logarithmic scale. Symbol colour and line colour are equal for the same value of n_{sep}.

depends on the ratio of density to temperature pedestal width.

$$
\begin{aligned}
H_{eff} &= H_{av} + \Delta H_{\nu^*} + \Delta H_s \\
H_{av} &= 0.41 \\
\Delta H_{\nu^*} &= -4.07 \times 10^{-2}\left(\frac{B_T n_{sep}}{3.726 \times I_p T_{sep}} - 1\right) \\
\Delta H_s &= \frac{H_s^+ - H_s^-}{2} x_s + \frac{H_s^+ + H_s^-}{2} x_s^2 \quad x_s = \frac{\ln(w_n/w_T)}{\ln(3)} \\
H_s^+ &= -5.89 \times 10^{-2} \\
H_s^- &= 4.92 \times 10^{-1}(\ln(f_T) - 1) - 9.51 \times 10^{-2}\ln(f_T)^2
\end{aligned}
\tag{18}
$$

The ΔH_{ν^*}-term was introduced in the fit to account for the reduced temperature screening at high collisionalities which only appears at the plasma edge near the separatrix (see Fig.2). This causes only a small change of H_{eff} between -0.03 at low to 0.03 at high ν^*. Here, $B_T n_{sep}/(I_p T_{sep})$ was used as a proxy for the ν^* variation that only depends on profile parameters. At the edge, Z_W^2 increases about linearly with T such that the usual $1/T^2$-scaling of ν^* is replaced by $1/T$. The units in eq.(18) are $[I_p]$=MA, $[B_T]$=T, $[n_{sep}]$=$10^{19}\mathrm{m^{-3}}$ and $[T_{sep}]$=keV.

The shape correction ΔH_s is zero for $w_n{=}w_T$, it reduces to $H_s^+{=}$-0.06 at $w_n{=}3w_T$ and increases for lower density widths up to $H_s^-{=}$0.06-0.14 for $w_n{=}w_T/3$. H_s^- is lowest for low values of f_T. ΔH_s is caused by the strong increase of Z_W with temperature and the shape correction of H_{eff} reflects the proportionality of H_{eff}^* with $\langle Z_W^T \rangle / \langle Z_W^n \rangle$. A given temperature increase in the ETB sets the range of tungsten charges that appear in the ETB and $\langle Z_W^T \rangle$ is almost constant independent of the width of the temperature pedestal. Furthermore, if density and temperature pedestal have the same width also $\langle Z_W^n \rangle$ will not depend on the choice of the width of the density pedestal and H_{eff} is almost identical for all widths as long as $w_n = w_T$. However, for $w_n < w_T$, only the lower charges contribute to $\langle Z_W^n \rangle$, while further inward, where Z_W is still increasing

with T, the normalised density gradient is already zero and $\langle Z_W^n \rangle$ will be lower than $\langle Z_W^T \rangle$. Thus, $H_{eff}^* = H \langle Z_W^T \rangle / \langle Z_W^n \rangle$ increases in this case, i.e. the effective temperature screening across the whole ETB rises since the normalised temperature gradient acts on higher charged W than the normalised density gradient. For $w_n > w_T$, the outward directed T-gradient term acts on all charges in the ETB since Z_W is rising with T; in this case, however, the inward pinch term driven by the density gradient is weighted with the maximum tungsten charge for most of the ETB radial extent, such that the term $\langle Z_W^T \rangle / \langle Z_W^n \rangle$ and H_{eff}^* is reduced accordingly. Thus, the scaling of the true H_{eff} can be well understood by the behaviour of H_{eff}^*, i.e. the approximate expression used in eq.(17).
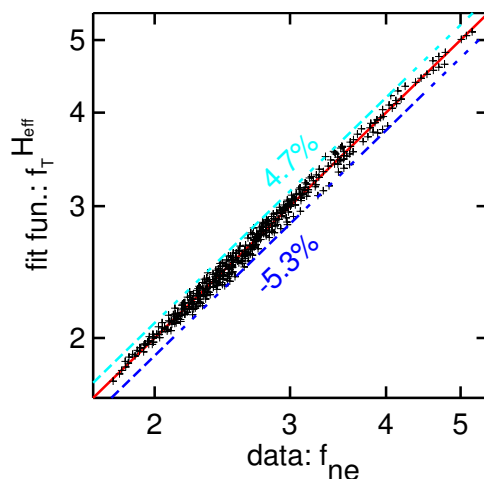
Figure 4. Electron density ratios f_{ne} that lead to $f_W = 1$. The values from the fit function defined in eq.(18) are plotted against the corresponding f_{ne} values from the data set for all profile parameters and all currents and toroidal fields.

The H_{eff}-function as given in eq.(18) yields a very good fit to the f_{ne} values at which f_W is unity as can be seen in Fig.4. The relative deviation of the fitted f_{ne} from the data is between -5.3% and 4.7% and the absolute value of this deviation is on average 1.6%. When only using a constant H_{av}, the deviations are between -38% and 19% respecively.

The fit function for H_{eff} can be applied for any H-mode parameters in ITER to calculate the density pedestal profile which delivers $f_W = 1$. At first, f_T is computed via eq.(8), eq.(9) and eq.(10) from the temperature parameters. When n_{sep} and w_n is given, eq.(18) delivers H_{eff} and the corresponding f_{ne} yields $n_{ped}(f_W = 1)$ from eq.(7). Density profiles which have a higher n_{ped} than $n_{ped}(f_W = 1)$ lead to W peaking, while lower values of n_{ped} provoke hollow W-profiles. Alternatively, we can determine $n_{sep}(f_W = 1)$ for a given n_{ped}. To this end, we start again by computing f_T from the temperature parameters and then the corresponding H_{eff}, which is first evaluated without the ΔH_{ν^*}-correction, delivers f_{ne} and via eq.(7) a starting value for n_{sep}. In the next iterations, the ΔH_{ν^*}-correction is included taking n_{sep} from the previous iteration, which quickly
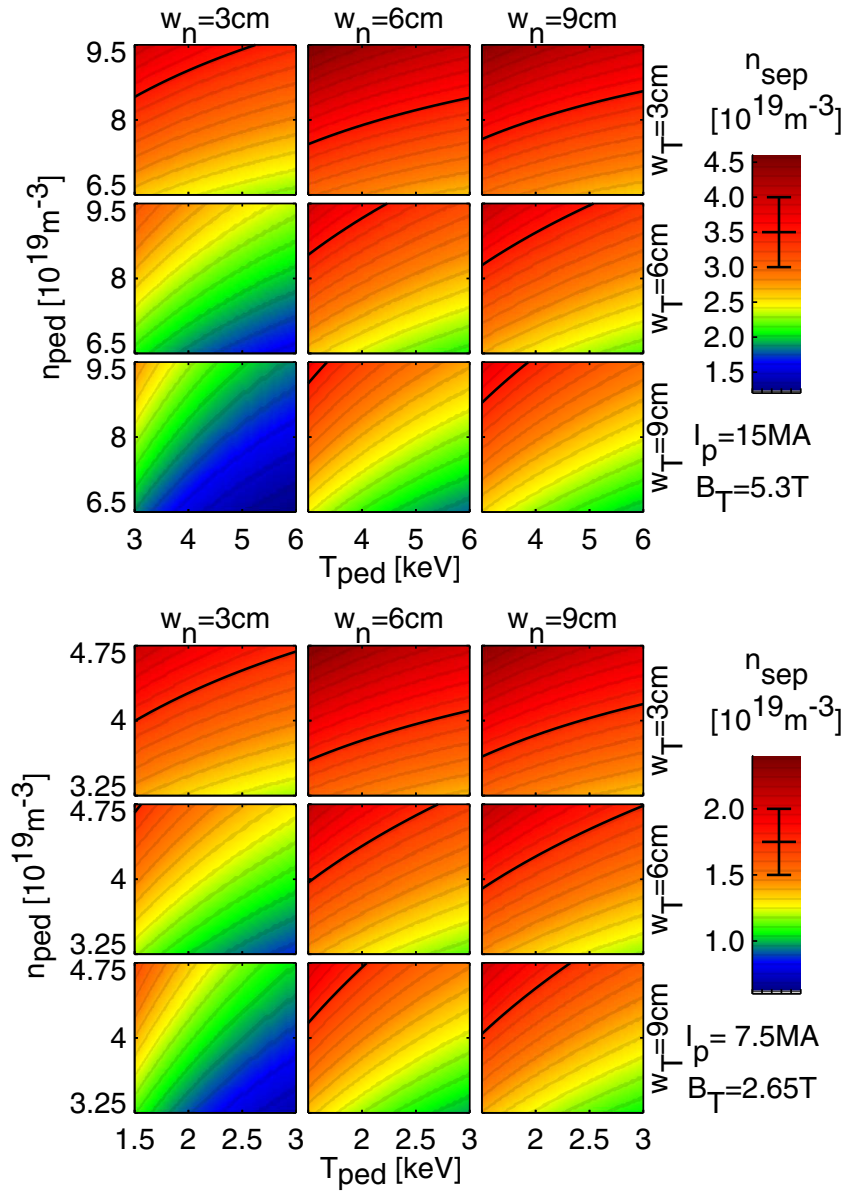
Figure 5. Separatrix densities leading to equal tungsten densities at the edge and the pedestal top for a range of pedestal densities and temperatures and pedestal widths in 15MA/5.3T and 7.5MA/2.65T DT H-modes in ITER. For higher n_{sep} values, neoclassical transport leads to hollow W-profiles in the ETB and vice versa. The black lines give an estimate of the minimum n_{sep} values being required to control the power exhaust for these two ITER scenarios [33, 13] (uncertainty interval is shown in the colour scale). Thus, all parameter combinations leading to a colour below this minimum value correspond to conditions in which when divertor power load control is satisfied in ITER it is also ensured that W-transport in the ETB will be outward-drift dominated and vice versa.

converges to the final value for $n_{sep}(f_W=1)$. Now, density profiles with n_{sep} below $n_{sep}(f_W=1)$ lead to W peaking, and higher values of n_{sep} lead to the favourable regime with neoclassical outward drift of W.

Fig.5 shows colour maps of these separatrix densities $n_{sep}(f_W=1)$ for two currents and fields as a function of T_{ped} and n_{ped} for all choices of the width-parameters w_n and w_T. The three maps on the diagonal of Fig.5 are for equal width of density and temperature pedestal $w_n = w_T$ and look rather similar to each other. Larger separatrix densities are required in the upper right boxes where $w_n > w_T$ and lower separatrix densities are sufficient for $f_W=1$ when $w_n < w_T$. The reason for this behaviour has been given above during the discussion of the ΔH_s-term in eq.(18).

In Fig.5, we also indicate the minimum values for n_{sep} (3-4×10^{19}m^{-3} for 15MA/5.3T and 1.5-2×10^{19}m^{-3} for 7.5MA/2.65T) which have to be achieved to control the power exhaust and W sputtering at the divertor in ITER [33, 13]. These minimum densities can be found in the colour scales as black lines with uncertainty intervals and again in each map as long as the corresponding density appears in the specific map.

The prevailing part of the scanned parameter space requires lower n_{sep} values to get into the regime of outward drift dominated W-transport in the ETB than for divertor power load/W sputtering control, as can be seen from the areas below the black lines in the individual colour maps. Only for a wide density and narrow temperature pedestal width (upper right boxes in Fig.5), about half of the parameter combinations lead to a situation with dominating neoclassical inward pinch at satisfactory divertor power load control.

6. Scaling of the diffusion coefficient of W

For all runs of the parameter scan, i.e. including the n_{sep} variations, the radially averaged diffusion coefficient of tungsten was calculated. The obtained diffusion coefficients are in the range of $D_{W,neo}$=(0.9-8)×10^{-2} m^{2}s^{-1}. The Pfirsch-Schlüter term is the dominant contribution to the neoclassical diffusion coefficient and is roughly given by $D_{W,PS} = 2q^2 D_{W,CL}$. A simple function that leads to a reasonably good fit is based on the radially averaged value of $n_e/\sqrt{T}$, i.e. the density and temperature scaling of the classical diffusion coefficient, and the plasma current I_p that enters via the q^2 dependence of the Pfirsch-Schlüter term and the inverse proportionality of the classical diffusion coefficient with the square of the toroidal field: $D_{W,CL} \propto B_T^{-2}$.

$$\langle D_{W,neo}\rangle = 0.63\frac{m^2}{s}\Big[\Big(\frac{MA}{I_p}\Big)^2\Big\langle\frac{n_e}{10^{19}m^{-3}}\sqrt{\frac{keV}{T}}\Big\rangle\Big]^{0.89} \tag{19}$$

This function reproduces the data set with a maximum deviation of ±12% as can be seen in Fig.6.
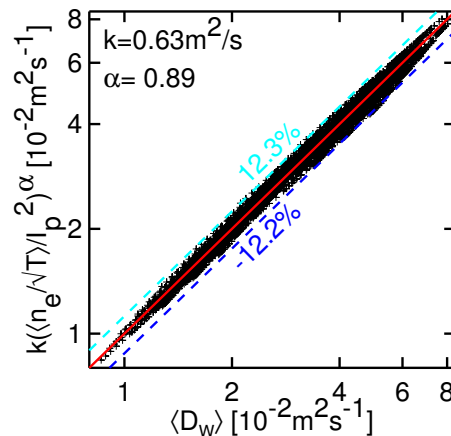
Figure 6. Radially averaged diffusion coefficients of tungsten: The values from the fit function defined in eq.(19) are plotted against the corresponding values from the data set for all profile parameters and all currents and toroidal fields.

I_p=15 MA, B_T=5.3 T, w_n=w_T=6 cm, T_{ped}=4.5 keV, n_{ped}=8×10^{19}m^{-3}					
$c_{He}[\%]$	1	1.5	2	2.5	3
$c_{Be}[\%]$	1	1.5	2	2.5	3
$c_{Ar}[\%]$	0.05	0.075	0.1	0.125	0.15
Z_{eff}	1.29	1.43	1.57	1.71	1.84
for n_{sep}=2.9×10^{19}m^{-3}					
$\nu^*\epsilon^{3/2}$	5.8	6.9	8.0	9.1	10.2
D_{neo} [m^2/s]	0.012	0.014	0.017	0.019	0.022
$v_{\nabla n}/D_{neo}$ [m^{-1}]	-115	-97.1	-84.7	-75.5	-68.5
$v_{\nabla T}/D_{neo}$ [m^{-1}]	119	98.8	84.3	73.3	64.7
$n_{sep}(f_W = 1)$ [10^{19}m^{-3}]	2.76	2.82	2.90	2.99	3.08

Table 2. For the mean values of the scanned parameters at I_p=15 MA and B_T=5.3 T, a variation of the impurity concentrations lead to the listed changes of the transport coefficients.

7. Sensitivity of the scalings to the impurity composition

A variation of the impurity concentrations around the chosen parameters for the database has been performed. The concentrations for the data base were 2% for He and Be and 0.1% for Ar and a variation has been considered from 1% to 3% for He and Be and from 0.05% to 0.15% for Ar. These values and the corresponding Z_{eff} are shown in the upper lines in Tab.2 for 15 MA/5.3T ITER Q=10 plasmas. The concentration of W was kept at 5×10^{-6} and the contribution of W to Z_{eff} is below 0.01.

The other fixed parameters are given in the first line of the table. When fixing the separatrix density to n_{sep}=2.9×10^{19}m^{-3}, we can compare the influence of the

impurity concentrations on the collisionality and the transport coefficients of tungsten. The collisionality increases with rising impurity concentrations by about a factor of 2 and so does the radially averaged diffusion coefficient. The contributions to the drift parameter, i.e. the drift due to the normalised density gradient and the drift due to the normalised temperature gradient, are shown in the following lines. The magnitude of both contributions decreases with increasing impurity concentrations. This decrease is due to the proportionality of the drifts with Z_W/Z_i, which decreases when collisions with higher charged impurity elements contributes more to the total collision frequency of tungsten such that Z_i increases. The outward directed temperature part decreases a little more rapidly than the inward directed density part, indicating that the PS temperature screening gets worse with increasing collisionality in the PS collisionality regime as already discussed in section 2. This effect finally leads to a slight increase of the separatrix density that is needed to have a tungsten density ratio of 1 $n_{sep}(f_W = 1)$. In this example, $n_{sep}(f_W = 1)$ increases by 2% for an increase of Z_{eff} by 0.1.

8. Reversal of Pfirsch-Schlüter temperature drift

It is known that the Pfirsch-Schlüter temperature screening reduces with rising collisionality. It can eventually reverse sign at very high collisionalities, such that the outward directed drift due to the normalised temperature gradient changes sign and becomes inward directed. Here, this transition point shall be quantified for ITER. For the standard magnetic equilibrium (B_T=5.3 T, I_p=15 MA), a radial position in the ETB: ρ_{pol}=0.99 (equal to x=2.2 cm from the separatrix) was chosen to perform an artificial temperature variation between 50-1000 eV in order to cause a large change of the collisionality of tungsten. The density was kept at a constant value of n_e=2×10^{19}m^{-3}. The impurity composition was again at the standard settings (He and Be:2%, Ar: 0.1% and W: 5×10^{-6}).

In the upper box of Fig.7, the temperature variation and the corresponding variation of the tungsten charge is depicted. Also the mean charge of Ar decreases with temperature such that Z_{eff} is slightly decreasing with temperature as well. The abscissae in Fig.7 are proportional to the collisionality of tungsten: $\nu^* \epsilon^{3/2} = qR_0/\lambda_{mfp}$. The PS-limit corresponds to $\nu^* \epsilon^{3/2}$=1. All collisionalities are deep in the PS-regime. In the lower box of Fig.7, the drift parameters due to the temperature gradient $v_{\nabla T}/D$ are shown. The blue line gives the purely classical drift parameter $v_{\nabla T,CL}/D_{CL}$ and the red line shows the PS values $v_{\nabla T,PS}/D_{PS}$, while the black line represents the total collisional drift parameter $(v_{\nabla T,CL}+v_{\nabla T,PS})/(D_{CL}+D_{PS})$. The PS-term is the dominant contribution, since roughly $D_{PS} \approx 2q^2 D_{CL}$. At lower collisionalities, all drift parameters are decreasing with increasing ν^* due to the decrease of Z_W with temperature. However, at high collisionalities, the PS-term shows an extra decrease and eventually goes to negative values, while the classical drift parameter stays positive throughout the whole range. The total drift parameter changes direction from outward to inward at a collisionality slightly above $\nu^* \epsilon^{3/2}$=100. This corresponds to a temperature of 92 eV
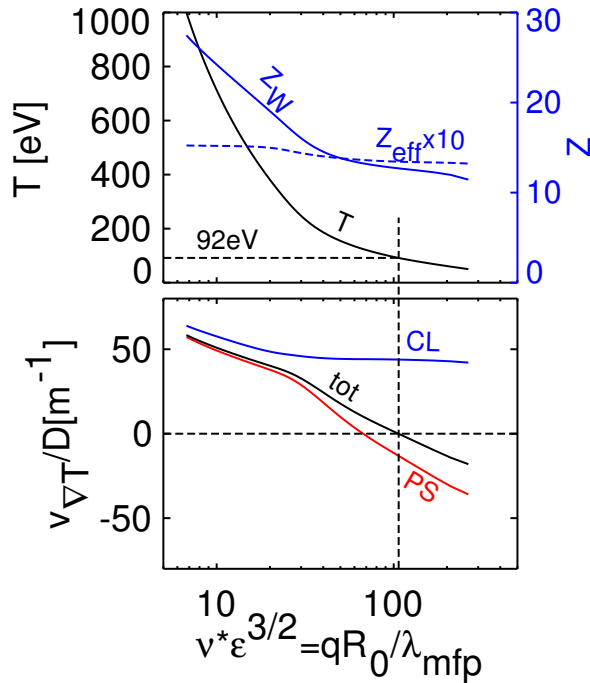
Figure 7. For a constant radial position ρ_{pol}=0.99, a large variation of temperature $T = T_i = T_e$ leads to a change of Z_W and Z_{eff} as is shown in the upper box versus the variation of the collisionality of tungsten. The lower box shows the corresponding effect on the drift parameter of tungsten due to the ion temperature gradient alone. It is positive (outward directed) at low collisionality and negative (inward directed) at high collisionality.

for the chosen parameters. This temperature is very low and will not occur in the ETB of ITER Q=10 plasmas, since it is roughly a factor of 3 lower than the average (electron + ion) separatrix temperature expected for such conditions in which the edge power flow amounts to 100 MW [13].

9. W transport in Helium plasmas

Helium plasmas at low field and currents (B_T= 2.65 T and I_p ≤7.5 MA) are foreseen in the ITER Research Plan to provide access to the H-mode in the non-active phase (with H and He plasmas) due to the lower H-mode power threshold in He compared to H plasmas and the available additional heating power installed in ITER [18]. Thus, the evaluation scheme to arrive at a scaling for H_{eff} and $D_{W,neo}$ was repeated for He plasmas but only plasmas with I_p=7.5 MA and B_T=2.65 T were considered. The used impurity composition was Be(2%), Ar(0.1%) and W(5×10^{-6}) with radially constant concentration profiles, i.e. the same as for DT plasmas.

When exchanging the main ion DT by He, the main effect is that the collision frequency with the main ion doubles because the He density is half the DT-density and $Z_{He}^2 n_{He} = 2Z_{DT}^2 n_{DT}$. Thus, the neoclassical diffusion coefficient increases and the

higher collisionality of tungsten leads to a reduction of the temperature drift (see section 8). For He plasmas, the values obtained for the diffusion coefficients are in the range of $D_{W,neo}=(3.4\text{-}14)\times10^{-2}\,\mathrm{m^2s^{-1}}$ and the fit-function for the radially averaged diffusion coefficient is almost a factor of 2 times the values from eq.(19), which represented the DT-case.

$$\langle D_{W,neo}\rangle = 1.04\frac{\mathrm{m^2}}{s}\Big[\Big(\frac{\mathrm{MA}}{I_p}\Big)^2\Big\langle\frac{n_e}{10^{19}\mathrm{m^{-3}}}\sqrt{\frac{\mathrm{keV}}{T}}\Big\rangle\Big]^{0.90} \tag{20}$$

This function reproduces the He data set with a maximum deviation of $\pm7\%$.

For H_{eff}, the helium data have been fitted with the same method as in section 5 and the corresponding fit function reads.

$$
\begin{aligned}
H_{eff} &= H_{av} + \Delta H_{\nu^*} + \Delta H_s \\
H_{av} &= 0.37 \\
\Delta H_{\nu^*} &= -1.12\times10^{-1}\Big(\frac{B_T n_{sep}}{3.275\times I_p T_{sep}} - 1\Big) \\
\Delta H_s &= \frac{H_s^+ - H_s^-}{2}x_s + \frac{H_s^+ + H_s^-}{2}x_s^2 \quad x_s = \frac{\ln(w_n/w_T)}{\ln(3)} \\
H_s^+ &= -5.05\times10^{-2} \\
H_s^- &= -4.22\times10^{-1}(\ln(f_T)-1) + 1.17\times10^{-1}\ln(f_T)^2
\end{aligned}
\tag{21}
$$

Here, the relative deviation of the fitted f_{ne} from the data is between -5.8% and 5.3% and the absolute value of this deviation is on average 2.4%. H_{eff} is generally lower than in eq.(18) and the higher collisionality in the helium plasma leads to about twice the sensitivity on collisionality changes, which is reflected in an increase of the proportionality factor in the equation for ΔH_{ν^*} by about a factor of 2.8. The shape correction term ΔH_s is slightly smaller than in the DT-case with H_s^+=-0.05 at $w_n=3w_T$ and H_s^-=0.05-0.12 at $w_n=w_T/3$.

Again, the fit function for H_{eff} has been used to calculate $n_{sep}(f_W=1)$ as a function of T_{ped} and n_{ped} for all choices of the width-parameters w_n and w_T and fig.8 shows the colour maps of these separatrix densities. The separatrix density required for successful ITER operation in He plasmas with a W divertor is expected to be in the range of 1-1.8$\times10^{19}\mathrm{m^{-3}}$ [34]. Density values in the lower part of the range are sufficient to provide an acceptable power load at the divertor, i.e. with maximum values lower than $10\,\mathrm{MWm^{-2}}$, while the higher values are required for control of divertor W sputtering by these He plasmas, i.e. $T_{e,div}\leq10\,\mathrm{eV}$. In Fig.8, n_{sep}=1.8$\times10^{19}\mathrm{m^{-3}}$ is shown as a black line in each map. The areas below the black lines (providing W sputtering control and outward drift of W in the ETB) are reduced compared to the same case in DT (lower graphs in fig.5). Especially for situations where the density has a larger pedestal width than the temperature, neoclassical transport provokes a peaking of W in the pedestal region for most of the edge profiles considered. When considering the lower separatrix density of $1\times10^{19}\mathrm{m^{-3}}$ (sufficient to provide divertor power load control but with sizeable divertor W sputtering), nearly the whole parameter space will lead to a
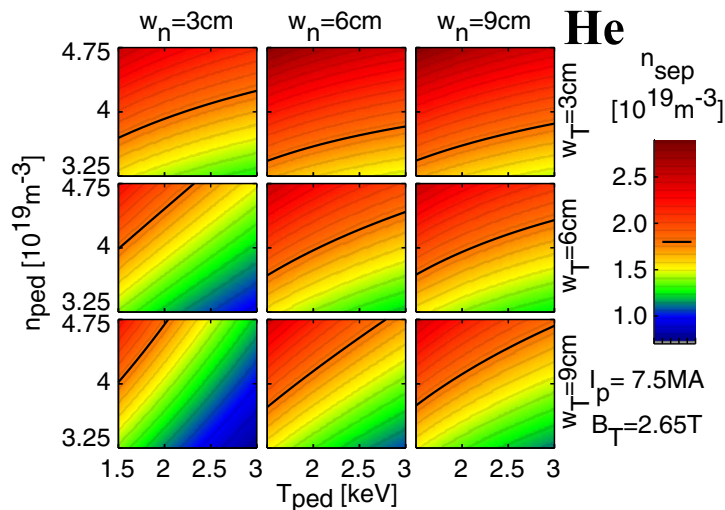
Figure 8. Separatrix densities leading to equal tungsten densities at the edge and the pedestal top for the case of a helium plasma at I_p=7.5 MA and B_T=2.65 T. The black lines give an estimate of the minimum n_{sep} values being required to control the divertor sputtering in the divertor, i.e. $T_{e,div} \leq 10$ eV.

neoclassical inward pinch and ELMs will play an essential role in controlling the W peaking in the H-mode edge transport barrier of such He H-mode plasmas in ITER.

10. Conclusions

It was already known from previous investigations on tungsten transport in the edge transport barrier region of ITER, that the collisional transport coefficients of W are very low leading to long time scales for equilibration of the W density profile in the ETB region [12]. These equilibration times are much longer than the ELM repetition times, which can be achieved with the ITER schemes for ELM control [35]. Thus, the transport during these controlled ELMs is thought to be the dominant transport effect and, in agreement with experimental results from present day tokamaks, the temporally averaged W profile should not show a strong peaking in the ETB of ITER H-mode plasmas.

The major finding of the study described in this paper is that the radial convection velocity of tungsten is outward directed for most of the edge plasma profiles considered for a wide range of ITER operational scenarios. This is due to a combination of the high pedestal temperatures expected in ITER and the high separatrix densities required for divertor power load and W sputtering control, which make the outward directed temperature screening term to be the predominant contribution of the collisional convection. Therefore, the achievement of the density and temperature profiles, which deliver optimum plasma performance in DT and appropriate divertor plasma conditions for power exhaust and W sputtering control in ITER, also ensures optimum collisional radial transport of tungsten leading to hollow tungsten density profile in the edge

transport barrier. Therefore, optimisation of W transport in the ETB, for core W impurity control in ITER, is not expected to lead to additional requirements for the edge plasma conditions in ITER beyond those associated with divertor power load and W sputtering control and with the pressure limits from edge MHD stability. However, in helium H-mode plasmas, this very favourable effect of neoclassical transport is reduced and only about half of the plasma profiles considered yield an outward directed drift while the other half has an inward directed radial drift for conditions in which divertor plasma conditions are expected to be appropriate in these He plasmas.

Acknowledgement

Disclaimer

The views and opinions expressed herein do not necessarily reflect those of the European Commission and of the ITER Organization

References

[1] M. Keilhacker, G. Fussmann, G. von Gierke, J. Janeschitz, M. Kornherr, et al., in *Plasma Physics and Controlled Nuclear Fusion Research 1984*, volume 1, pages 71–85, Vienna, 1984, IAEA.

[2] K. Behringer, B. Denne, A. Edwards, N. Gottardi, M. von Hellermann, et al., in *Europhysics Conference Abstracts (Proc. of the 15th EPS Conference on Controlled Fusion and Plasma Physics, Dubrovnik, 1988)*, edited by S. Pesic and J. Jacquinot, volume 12B, part I, pages 338–341, Petit-Lancy, 1988, EPS.

[3] R. Giannella, K. Behringer, B. Denne, N. C. Hawkes, M. von Hellermann, et al., in *Europhysics Conference Abstracts (Proc. of the 16th EPS Conference on Controlled Fusion and Plasma Physics, Venice, 1989)*, edited by S. Segre, H. Knoeptel, and E. Sindoni, volume 13B, part I, pages 209–212, Petit-Lancy, 1989, EPS.

[4] N. Hawkes, Z. Wang, R. Barnsley, K. Behringer, S. Cohen, et al., in *Europhysics Conference Abstracts (Proc. of the 16th EPS Conference on Controlled Fusion and Plasma Physics, Venice, 1989)*, edited by S. Segre, H. Knoeptel, and E. Sindoni, volume 13B, part I, pages 79–82, Petit-Lancy, 1989, EPS.

[5] D. Pasini, R. Giannella, L. Lauro-Taroni, M. Mattioli, B. Denne-Hinnov, et al., Plasma Phys. Controlled Fusion **34**(5), 677–684 (1992).

[6] M. E. Perry, N. H. Brooks, D. A. Content, R. A. Hulse, M. A. Mahdavi, et al., Nucl. Fusion **31**(10), 1859–1875 (1991).

[7] J. E. Rice, J. L. Terry, J. A. Goetz, Y. Wang, E. S. Marmar, et al., Phys. Plasmas **4**(5), 1605–1609 (1997).

[8] T. Sunn Pedersen, R. S. Granetz, A. E. Hubbard, I. H. Hutchinson, E. S. Marmar, et al., Nucl. Fusion **40**(10), 1795–1804 (2000).

[9] R. Dux, Fusion Science and Technology **44**(3), 708–715 (2003).

[10] T. Pütterich, R. Dux, M. Janzer, R. McDermott, and ASDEX Upgrade Ream, Journal of Nuclear Materials **415**(1, Supplement), S334–S339 (2011).

[11] E. Viezzer, T. Pütterich, R. Dux, R. M. McDermott, and ASDEX Upgrade Team, Review of Scientific Instruments **83**(10), 103501 (2012).

[12] R. Dux, A. Janzer, T. Pütterich, and ASDEX Upgrade Team, Nuclear Fusion **51**(5), 053002 (2011).

[13] A. Kukushkin, H. Pacher, G. Pacher, V. Kotov, R. Pitts, et al., Nuclear Fusion **53**(12), 123024 (2013).

[14] R. Dux, V. Bobkov, A. Herrmann, A. Janzer, A. Kallenbach, et al., Journal of Nuclear Materials **390-391**, 858–863 (2009).

[15] G. J. van Rooij, J. Coenen, L. Aho-Mantila, S. Brezinsek, M. Clever, et al., Journal of Nuclear Materials **438, Supplement**, S42 – S47 (2013).

[16] E. Fable et al., Effect of Impurities and ELMs on the ITER Baseline Scneario, in preperation for Nuclear Fusion (2014).

[17] M. Balden, N. Endstrasser, P. Humrickhouse, V. Rohde, M. Rasinski, et al., Nuclear Fusion **54**(7), 073010 (2014).

[18] D. J. Campbell et al., in *Proc. of the 24th IAEA Fusion Energy Conference, San Diego, USA*, volume IAEA-CN-197, pages ITR/P1–18, Vienna, 2012, IAEA.

[19] S. P. Hirshman and D. J. Sigmar, Nucl. Fusion **21**(9), 1079–1201 (1981).

[20] P. Helander and J. Sigmar, *Collisional Transport in Magnetized Plasmas*, Cambridge Univ. Press, Cambridge, 1st edition, 2002.

[21] K. Wenzel and D. Sigmar, Nuclear Fusion **30**(6), 1117 (1990).

[22] G. Fußmann, A. R. Field, A. Kallenbach, K. Krieger, K.-H. Steuer, et al., Plasma Phys. Controlled Fusion **33**(13), 1677–1695 (1991).

[23] A. G. Peeters, Phys. Plasmas **7**(1), 268–275 (2000).

[24] W. A. Houlberg, K. C. Shaing, S. P. Hirshman, and M. C. Zarnstorff, Phys. Plasmas **4**(9), 3230–3241 (1997).

[25] T. Casper, Y. Gribov, A. Kavin, V. Lukash, R. Khayrutdinov, et al., Nuclear Fusion **54**(1), 013005 (2014).

[26] P. Maget, J.-F. Artaud, M. Becoulet, T. Casper, J. Faustin, et al., Nuclear Fusion **53**(9), 093011 (2013).

[27] M. N. A. Beurskens et al., Physics of Plasmas **18**, 056120 (2011).

[28] T. Eich, A. Leonard, R. Pitts, W. Fundamenski, R. Goldston, et al., Nuclear Fusion **53**(9), 093031 (2013).

[29] ITER Physics Expert Groups, Nucl. Fusion **39**(12), 2175–2235 (1999).

[30] G. Pacher, H. Pacher, G. Janeschitz, and A. Kukushkin, Nuclear Fusion **48**(10), 105003 (2008).

[31] A. Kallenbach, M. Bernert, R. Dux, L. Casali, T. Eich, et al., Plasma Phys. Control. Fusion **55** 124041 (2013).

[32] H. P. Summers, Atomic data and analysis structure users manual 2.6, http://www.adas.ac.uk/manual.php (2004).

[33] A. S. Kukushkin, H. Pacher, V. Kotov, G. Pacher, R. Pitts, et al., in *Proc. of the 23rd IAEA Conference, Fusion Energy, Daejon, Rep. of Korea*, pages IAEA–CN–180/ITR/P1–33, Vienna, 2010, IAEA.

[34] A. S. Kukushkin et al., in *Europhysics Conference Abstracts (CD-ROM, Proc. of the 40th EPS Conference on Plasma Physics, Espoo, Finland, 2013)*, edited by V. Naulin, C. Angioni, M. Borghesi, S. Ratynskaia, S. Poedts, et al., volume 37D of *ECA*, page P1.124, Geneva, 2013, European Physical Society.

[35] A. Loarte et al., Progress on the application of ELM control schemes to ITER scenarios from the non-active phase to DT operation, Nuclear Fusion **54**, 033007 (2014).